Research Article

Journal of Environmental Nanotechnology

Green-fabricated Cu–Ti Bimetallic Nanoparticles Derived from *Psidium guajava* Leaf Extract for Catalytic Hydrogen Generation

P. Priya[1], S. Mayakannan[2,3*], B. A. Brundha[4], L. R. Sujithra[5], R. Subbulakshmi[6] and S. Rakesh[7]

[1]Department of Computer Science and Engineering, M. Kumarasamy College of Engineering, Karur, TN, India
[2]Department of Mechanical Engineering, Saveetha School of Engineering, Saveetha Institute of Medical and Technical Sciences, Chennai, TN, India
[3]Department of Mechanical Engineering, Rathinam Technical Campus, Coimbatore, TN, India
[4]Department of Chemistry, Vel Tech High Tech Dr. Rangarajan Dr. Sakunthala Engineering College, Chennai, TN, India
[5]Department of Artificial Intelligence and Data Science, Sri Eshwar College of Engineering, Coimbatore, TN, India
[6]Department of Computer Science and Engineering, Karpagam Institute of Technology, Coimbatore, TN, India
[7]Department of Mechanical Engineering, Francis Xavier Engineering College, Tirunelveli, TN, India
Received: 05.07.2026 Accepted: 03.08.2026 Published: 30.09.2026
*kannanarchieves@gmail.com

ABSTRACT

In this investigation, Cu–Ti bimetallic nanoparticles were synthesized through a sustainable green route employing *Psidium guajava* leaf extract as the reducing and stabilizing agent. The XRD characterization indicated an average crystallite size of approximately 40 nm, whereas SEM observations revealed predominantly irregular structures together with a limited number of spherical particles. The elemental composition of Cu, Ti, and C was confirmed with EDX measurements, while Raman analysis verified the structural stability and formation of metal–oxygen bonds. The catalytic efficiency of the prepared nanoparticles was evaluated by varying reaction temperature, catalyst dosage, and the solution composition during $NaBH_4$ hydrolysis. Under 0.50 wt% NaOH, the catalyst exhibited a maximum hydrogen generation rate of 446.5 mL min^{-1} g^{-1}. Kinetic evaluation determined activation energy of 53.98 kJ mol^{-1} for Cu–Ti catalyst. Subsequently, machine learning techniques including Gaussian Process Regression, Light Gradient Boosting Machine (LightGBM), HistGradientBoosting, CatBoost, Support Vector Regression, Random Forest, and Extra Trees Regressor were implemented to estimate hydrogen generation performance. The experimental dataset was enhanced using polynomial, logarithmic, and interaction-based descriptors, while 5-fold cross-validation minimized overfitting during model training. Among the developed models, Gaussian Process Regression (R^2 = 0.9937) achieved the highest predictive capability, whereas LightGBM (R^2 = 0.9589) and CatBoost (R^2= 0.9584) also demonstrated reliable prediction performance. These findings indicate that, green-fabricated Cu–Ti nanoparticles provide efficient catalytic activity for hydrogen evolution, and that, advanced machine learning methods offer reliable prediction and optimization of hydrogen production. This combined experimental and computational strategy provides a valuable pathway for accelerating catalyst design toward sustainable clean-energy technologies.

Keywords: Green synthesis; Catalyst dosage; Catalytic activity; Optimization; Machine learning.

1. INTRODUCTION

The continued dependence on fossil fuels has created significant environmental and energy-related challenges, including pollution, climate change, and concerns over energy security. Recent advances in green nanotechnology have demonstrated that plant-derived extracts can serve as effective reducing and stabilizing agents for the sustainable synthesis of functional nanomaterials. For instance, Moringa oleifera-assisted TiO_2 nanocomposites have been synthesized through a green route and investigated for multifunctional applications (Hema *et al.* 2025). Ba–Fe dual-doped TiO_2 nanocomposites were green synthesized using *Psidium guajava* leaf extract through plant-mediated synthesis (Goyal *et al*. 2026). CeO_2 and Cu-doped CeO_2 nanoparticles (NPs) were successfully synthesized by *Psidium guajava* leaf extract, with structural and morphological properties confirmed by XRD, Scanning electron microscopy (SEM), and EDX (Mohamed *et al.* 2025). Highly stable copper NPs and graphene-based Cu nanocomposites were synthesized using *Psidium guajava* leaf extract through microwave-assisted and chemical reduction methods. Characterization by XRD, Raman, and FE-SEM confirmed the successful formation of the nanostructures, while nonlinear optical studies revealed that, the rGO–Cu composite possessed superior optical limiting performance (Akhil *et al.* 2025). A green TiO_2/Fe nanocomposite synthesized using *Psidium guajava* leaf extract was developed to enhance durability and multifunctional properties. The SEM and EDS analyses confirmed successful nanoparticle incorporation, with uniform elemental distribution (Rahman *et al.* 2025). Green-synthesized ZnO, Mg–Ti–ZnO and Ti–ZnO NPs

by *Psidium guajava* extract were developed (Naseer *et al.* 2023). Green-synthesized CuO/rGO nanocomposites were fabricated using *Psidium guajava* leaf extract to study dye degradation when exposed to natural sunlight. Raman spectroscopy confirmed successful CuO/rGO formation with a reduced bandgap, leading to enhanced degradation of methylene blue and Reactive Red 141, while pristine CuO NPs also demonstrated anticancer activity (Noorani *et al.* 2026). Green-synthesized silver NPs derived from *Psidium guajava* leaf extract were investigated using SEM and XRD to evaluate their morphology and crystalline structure (Raghupathy *et al.* 2024). Co_3O_4 NPs and rGO–Co_3O_4 nanocomposites were biosynthesized using *Psidium guajava* leaf extracts for electrocatalytic water splitting. Linear sweep voltammetry, Tafel slope, and double-layer capacitance analyses demonstrated that the non-calcined rGO-decorated Co_3O_4 nanocomposites exhibited superior oxygen evolution and hydrogen evolution reaction performance (Akram *et al.* 2025).

The integration of advanced analytical techniques and data-driven approaches has further broadened the scope of *Psidium guajava*-mediated nanomaterials. A multi-light source fluorescence imaging system integrating color and fluorescence images were developed for the non-destructive assessment of guava fruit quality and maturity. Partial Least Squares Regression accurately predicted soluble solid content and firmness, whereas the Support Vector Machine achieved 91% maturity classification accuracy (Lin *et al.* 2025). Metformin-conjugated ZnO NPs were green synthesized using *Psidium guajava* leaf extract to develop a multifunctional therapeutic nanoplatform (Mathew *et al.* 2026). Green-synthesized AgNPs and Ag–fluconazole hybrid nanoformulations prepared using *Psidium guajava* leaf extract were evaluated for controlling *Fusarium* wilt in chickpea. Particle size analysis confirmed nanoscale formulations, while the hybrid nanoformulation exhibited enhanced antifungal activity and increased antioxidant enzyme responses (Warkad *et al.* 2026). NiO nanoparticles were green synthesized using *Psidium guajava* leaf extract through nickel nitrate reduction process with different annealing temperatures (Ganesan *et al.* 2025). A green nZVI@Chitosan nanocomposite from *Psidium guajava* leaf extract and chitosan was developed for biofilm control and antimicrobial applications (Dokania *et al.* 2026). A biodegradable CTS/PVA/SeGO composite film incorporating selenium NPs synthesized using *Psidium guajava* leaf extract was developed for sustainable packaging applications (Tuyen *et al.* 2026).

Furthermore, *Psidium guajava*-based nanomaterials have demonstrated remarkable potential in multifunctional biomedical, photocatalytic, and catalytic systems. CuO NPs and CuO/ZnO nanocomposites were green synthesized using *Psidium guajava* leaf extract for biomedical applications. The SEM analysis confirmed nanoscale particle morphology, while the CuO/ZnO nanocomposite exhibited enhanced antibacterial, antioxidant, and selective anticancer activity compared with CuO nanoparticles (Alsalamah *et al.* 2026). Microwave-assisted green synthesis of Cu NPs using *Psidium guajava* leaf extract produced highly active multifunctional nanomaterials. Photoluminescence and Dynamic Light Scattering analyses optimized nanoparticle formation, and the Cu NPs demonstrated rapid photocatalytic dye degradation, photothermal conversion, and strong antibacterial activity (Soundarya *et al.* 2026). The XRD analysis of the green-synthesized hematite and magnetite NPs prepared using *Psidium guajava* and *Moringa oleifera* leaf extracts confirmed the formation of highly crystalline iron oxide phases without detectable impurities. The diffraction patterns indicated good crystallinity with an estimated crystallite size of 20–30 nm, in agreement with the FESEM results (Begum *et al.* 2025). A theoretical investigation based on density functional theory explored Cu-based FCC–FCT alloys for selective CO_2 electroreduction to ethanol. A novel charge disparity index was proposed as an electronic descriptor to predict ethanol formation while suppressing competing hydrogen evolution and C_1 product pathways (Iqbal *et al.* 2026). Uniformly dispersed CeO_2–MgO supports were synthesized by a spray pyrolysis-assisted EISA method to investigate the behavior of supported Cu NPs. The study demonstrated that controlled Cu dispersion significantly enhanced catalyst properties, providing insights for high-temperature shift reactions and waste-to-hydrogen production (Kim *et al.* 2025). A plasmon-driven Au/Cu nanostructured photocatalyst was developed for low-temperature ammonia decomposition to generate hydrogen under visible light (Bui *et al.* 2026). Magnetically separable Cu@Fe_3O_4: PES catalyst beads were designed for ammonia borane hydrolysis and tandem organic reduction (Shingole *et al.* 2026).

To the best of current knowledge, no previous investigation has comprehensively examined the catalytic performance of green-synthesized Cu–Ti bimetallic nanoparticles derived from *Psidium guajava* leaf extract for $NaBH_4$ hydrolysis in combination with experimental and machine learning (ML)-based prediction. Accordingly, Cu–Ti nanoparticles were synthesized through environmentally friendly green route using *Psidium* leaf extract and systematically characterized by analytical methods. Influence of key operating variables, including catalyst dosage, $NaBH_4$ concentration, NaOH concentration, and reaction temperature, hydrolysis process, was thoroughly evaluated and activation energy was determined through kinetic analysis. The experimental dataset was interpreted by kernel-based, probabilistic, and ensemble ML algorithms, providing an integrated framework for development of data-driven optimization and sustainable catalytic materials of hydrogen production systems.

2. MATERIALS AND METHODOLOGY

2.1 Materials

Fresh *Psidium guajava* leaves were collected from healthy plants in accordance with the principles of green chemistry and environmental sustainability. The harvested leaves were thoroughly cleaned to eliminate adhering impurities and subsequently prepared for experimental use owing to their abundant phytochemical constituents, particularly phenolic and flavonoid compounds. Copper (II) chloride dihydrate ($CuCl_2 \cdot 2H_2O$) was used as the copper precursor, titanium (IV) isopropoxide as the titanium precursor, $NaBH_4$ as the hydrogen source, and NaOH as the alkaline medium. These were procured from Star Scientific, Erode. Throughout the experimental work, high-purity distilled water was employed for solution preparation and reaction processes to ensure reliable and reproducible results.

2.2 Preparation of *Psidium guajava* Leaf Extract

Fresh *Psidium guajava* leaves were thoroughly washed with distilled water to eliminate dust, surface contaminants, and other impurities that could influence the synthesis process. The cleaned leaves were air-dried, pulverized, and sieved to obtain a fine powder suitable for extraction. The preparation of leaf extract followed the procedure mentioned in an earlier study (Abdellatif *et al.* 2026). To efficiently recover the phytochemical constituents, 30 g of powdered leaves was transferred into 500 mL flask containing 350 mL of DI water. The suspension was heated under reflux for 1 hour to facilitate the extraction of bioactive compounds. During this process, phenolic compounds, flavonoids, polyphenols, and organic acids present in the leaves were released into the aqueous medium. These naturally occurring metabolites function as stabilizing and reducing agents during formation of Cu–Ti NPs by promoting metal-ion reduction and preventing particle agglomeration. The resulting extract was allowed to cool to ambient temperature and filtered using 0.45 µm cellulose filter paper to eliminate residual solids.

2.3 Preparation of Cu−Ti Nanoparticles

Cu–Ti nanoparticles were synthesized by eco-friendly green approach using *Psidium guajava* leaf extract as the stabilizing and reducing medium. For the synthesis, appropriate quantities of $CuCl_2 \cdot 2H_2O$ and titanium(IV) isopropoxide were mixed at a Cu:Ti molar ratio of 1:1 and dispersed in 100 mL of the prepared leaf extract. The reaction mixture was continuously stirred for 24 hours at ambient temperature to obtain a uniform suspension. The phytochemicals present in the leaf extract promoted the reduction of metal precursors and facilitated the formation of Cu–Ti NPs. Likewise, Cu–Ti bimetallic nanocatalysts were successfully synthesized in the previous work through a plant-mediated green synthesis method (Saeed *et al.* 2019). The resulting nanoparticles were collected by filtration using 0.45 µm cellulose filter paper, followed by repeated washing with DI water to eliminate residual impurities. Purified NPs were dried at 105 °C in a nitrogen atmosphere for 3 hour and preserved in airtight containers for subsequent catalytic evaluation and characterization during $NaBH_4$ hydrolysis.

2.4 Characterization of Cu−Ti Nanoparticles

The Cu–Ti NPs were characterized using advanced analytical techniques to evaluate their physicochemical properties. The crystalline phase and structural characteristics were analyzed by X-ray diffraction employing Bruker D8 diffractometer. Surface morphology together with the elemental distribution of Cu–Ti NPs was examined using scanning electron microscopy integrated with Energy-dispersive X-ray spectroscopy (EDS). Furthermore, structural features and bonding characteristics of the synthesized nanoparticles were assessed through Raman spectroscopy.

2.5 Catalytic Hydrolysis Performance

Hydrogen evolution was quantified by water displacement technique. The catalytic efficiency of the synthesized Cu–Ti nanoparticles toward $NaBH_4$ hydrolysis was investigated using a laboratory-scale hydrogen generation apparatus (Jagadeesha *et al.* 2026). To establish the optimum operating conditions, experiments were carried out by varying the concentrations of $NaBH_4$ and NaOH, together with different catalyst loadings. For each experimental run, 20–80 mg of the Cu–Ti catalyst was introduced into the reaction flask. Initially, 10 mL of 1–5 wt% sodium borohydride solution without NaOH was maintained in thermostatically controlled water bath at 30 °C. After identifying optimum reaction, the volume of hydrogen released was recorded as function of reaction time at operating temperatures of 25–55 °C.

The hydrogen generation rate (HGR) values were calculated from slope of linear section of hydrogen evolution curve using Eq. (1).

$$\text{HGR} = \frac{\text{Hydrogen generation volume (mL)}}{\text{time (min)} \times \text{catalyst mass (g)}} \quad \ldots (1)$$

2.6 Calculation of Activation Energy

The hydrolysis kinetics of $NaBH_4$ in the presence of the synthesized Cu–Ti NPs was interpreted using an nth-order kinetic model. Based on this approach, the volumetric reaction rate can be expressed as Eq. (2):

$$-r_A = -\frac{dCA}{dt} = kC^n A \quad \ldots (2),$$

where C is the concentration of the reactant, k is the kinetic rate constant, r indicates the reaction rate, and n defines the order of the reaction.

3. RESULTS AND DISCUSSION

3.1 Characterization

X-ray diffraction is a reliable technique for identifying crystalline phases, structural characteristics, and crystallite size of nanomaterials. The diffraction pattern of synthesized Cu–Ti NPs is presented Fig. 1a. Green synthesis route employing *Psidium* leaf extract effectively promoted formation of crystalline Cu–Ti NPs. The diffraction profile exhibited characteristic reflections at 2θ values of 25.3°, 35.1°, 43.3°, 50.4°, 62.5°, 74.1°, and 77.2°, which were indexed to the (111), (200), (111), (200), (211), (220), and (311) crystallographic planes, respectively. These reflections confirm the successful formation of the Cu–Ti bimetallic nanostructure without noticeable impurity phases. The intense diffraction peaks indicate good crystallinity and an ordered crystal framework produced through the green synthesis process. Furthermore, the XRD results demonstrate the effective incorporation of copper and titanium species within the nanoparticle matrix, suggesting strong structural interaction between both metallic components. Such a crystalline architecture provides abundant active sites and enhanced structural stability, making the synthesized NPs highly suitable for catalytic hydrogen generation through $NaBH_4$ hydrolysis. As reported in a previous analysis, biogenic SnO_2–CuO–SA and SnO_2–NiO–SA nanocomposites synthesized using *Psidium guajava* leaf extract exhibited a tetragonal rutile crystal structure, as confirmed by XRD analysis. The average crystallite sizes were 67.8 nm for SnO_2–CuO–SA and 58.1 nm for SnO_2–NiO–SA, indicating the successful formation of highly crystalline nanocomposites (Balasubramaniyan *et al.* 2025).

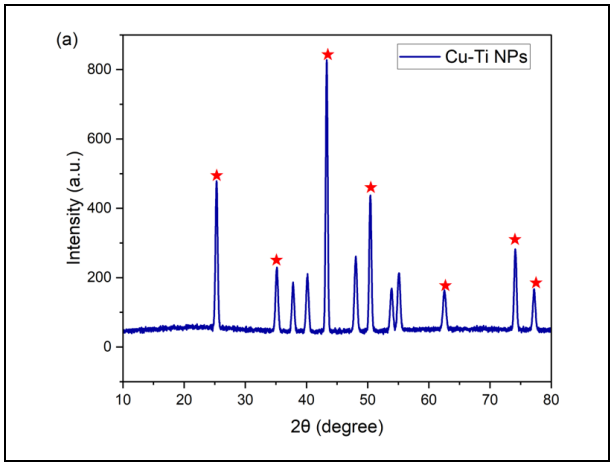

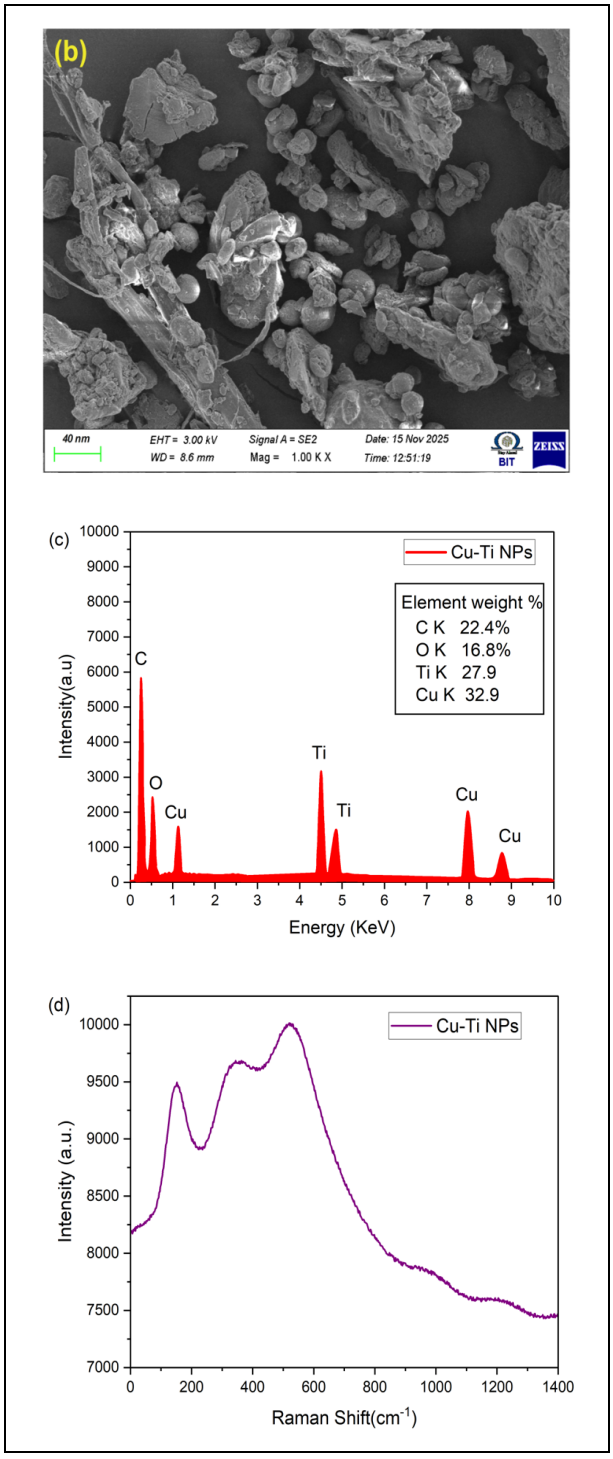

Fig. 1: Characterization of Cu–Ti NPs (a) XRD pattern, (b) SEM micrograph, (c) EDS spectrum and (d) Raman spectrum

The average crystallite size of the prepared Cu–Ti nanoparticles was evaluated from the X-ray diffraction pattern.

$$D = \frac{k\lambda}{\beta \cos\theta} \quad \ldots (3)$$

Using the Debye–Scherrer approach (Eq. 3), the average crystallite size of the synthesized Cu–Ti NPs was estimated to be approximately 40 nm, confirming the formation of uniformly distributed nanocrystalline particles. Scanning electron microscopy was employed to analyse surface morphology, particle size, and structural characteristics of green-synthesized nanoparticles. In addition to morphological evaluation, SEM provides valuable information regarding particle uniformity, structural integrity, and the effectiveness of the synthesis strategy. The SEM micrographs of the Cu–Ti NPs are presented in Fig. 1b. The images reveal that the synthesized particles predominantly exhibited quasi-spherical morphology with occasional rod-like features. A slight variation in particle shape and size was observed, reflecting the influence of the green synthesis process on nanoparticle growth. Particle size analysis indicated that the nanoparticles remained below 100 nm, providing a high surface-to-volume ratio that is advantageous for catalytic $NaBH_4$ hydrolysis. Nevertheless, partial particle agglomeration was evident, which is commonly attributed to the elevated surface energy of nanoscale materials and attractive Van der Waals interactions between adjacent particles. Such aggregation is frequently encountered during the synthesis of metallic nanoparticles and may reduce accessible catalytic active sites. Therefore, minimizing agglomeration through optimized synthesis conditions and the stabilizing action of phytochemicals present in *Psidium guajava* leaf extract can further improve the dispersion and catalytic performance of the Cu–Ti NPs. Energy-dispersive X-ray spectroscopy was carried out to analyse the elemental composition of synthesized nanoparticles. The EDS results verify the successful incorporation of copper and titanium within the nanostructure and assess the compositional uniformity achieved during the green synthesis process. The EDS spectrum of synthesized Cu–Ti NPs is presented Fig. 1c.

Energy-dispersive X-ray spectrum confirms the successful synthesis of Cu–Ti NPs through green synthesis route employing *Psidium guajava* leaf extract. The elemental analysis identified only Cu, Ti, and C, confirming the formation of the desired bimetallic nanostructure without detectable impurity elements. The carbon signal originates from bioactive phytochemicals, including polyphenols, flavonoids, and other carbon-containing metabolites naturally present in *Psidium guajava* leaf extract. These compounds function as both surface-stabilizing and reducing agents during nanoparticle formation, promoting uniform nucleation while suppressing excessive particle growth. According to Fig. 1c, elemental composition of synthesized Cu–Ti NPs was 32.9 wt% Cu, 27.9 wt% Ti, and 22.4 wt% C. These results verify successful addition of copper and titanium into nanostructure. Relatively higher copper content is attributed to the faster reduction kinetics of Cu^{2+} ions compared with titanium precursor species under the action of the phytochemicals present in the leaf extract, resulting in more efficient copper deposition during the synthesis process. The significant carbon content further indicates the adsorption of plant-derived organic molecules onto the nanoparticle surface, enhancing colloidal stability and minimizing nanoparticle aggregation. Thus, the EDS findings demonstrate that the green synthesis strategy produced chemically homogeneous and structurally stable Cu–Ti NPs with high purity, indicating their suitability as efficient catalysts for $NaBH_4$ hydrolysis and hydrogen generation. A previous work has demonstrated that, the biogenic CuO NPs synthesized by *Psidium* leaf extract exhibited oval and platelet-shaped morphologies with particle sizes ranging from 40–150 nm, as revealed by FE-SEM analyses and confirmed successful formation of high purity NPs by EDS analysis that verified the presence of copper and oxygen elements (Sathiyavimal *et al.* 2021).

Raman spectroscopy is an effective analytical technique for investigating the molecular structure, chemical bonding, and lattice characteristics of nanomaterials. It provides valuable insight into the vibrational behavior of metal–oxygen frameworks and the structural integrity of synthesized NPs. The Raman spectrum of prepared Cu–Ti NPs is presented in Fig. 1d, where Raman shift is expressed in cm^{-1}. Two prominent Raman bands were observed at approximately 152 cm^{-1} and 630 cm^{-1}, corresponding to the characteristic lattice vibrations of the synthesized nanostructure. The low-frequency band at 152 cm^{-1} is attributed to Cu–O–Ti lattice and reflects the ordered crystalline arrangement of the bimetallic framework. This vibration is also influenced by nanoscale particle dimensions and phonon confinement effects. The intense band centered at 630 cm^{-1} is attributed to the Ti–O stretching vibration, together with contributions from Cu–O bonds, confirming the successful formation of the mixed metal–oxide network. These Raman features indicate strong interaction between copper and titanium species within the nanostructure. Furthermore, the phytochemical constituents of *Psidium guajava* leaf extract, including polyphenols and flavonoids, act as stabilizing and reducing agents for nanoparticle formation, promoting the development of stable metal–oxygen linkages. The presence of these biomolecules is consistent with the carbon signal observed in the EDS analysis, further supporting the successful green synthesis of chemically stable Cu–Ti NPs. Prior investigation employed Raman spectroscopy to characterize the biogenic selenium nanoparticles (SeNPs) synthesized using *Psidium guajava* leaf extract, where XRD and XPS analyses

confirmed their structural features. The Raman results supported the successful formation of SeNPs and complemented the physicochemical characterization of the adsorbent used for efficient Sb (III) removal (Ran *et al.* 2024).

3.2 Applications of $NaBH_4$ Hydrolysis

$NaBH_4$ exhibited a stable exothermic process under alkaline conditions, where NaOH significantly influences the reaction kinetics and catalytic performance. Therefore, the catalytic activity of the green-synthesized Cu–Ti NPs prepared using *Psidium guajava* leaf extract was systematically evaluated by varying the NaOH concentration from 0 to 2.00 wt%. Experiments were performed at 0, 0.25, 0.50, 1.00, 1.50, and 2.00 wt% NaOH to determine optimum alkaline condition for hydrogen generation during $NaBH_4$ hydrolysis (Fig. 2a).

The influence of NaOH concentration hydrolysis of $NaBH_4$ was systematically investigated using the synthesized Cu–Ti NPs at identical experimental conditions. The catalytic hydrogen generation rate was 172.2 mL min^{-1} g^{-1} in the absence of NaOH. Increasing the alkaline concentration to 0.25 wt% enhanced the reaction rate to 446.5 mL min^{-1} g^{-1}, while the maximum hydrogen rate of 331.8 mL min^{-1} g^{-1} was achieved at 0.50 wt% NaOH. A further raise in NaOH concentration resulted at gradual decline in catalytic performance, with hydrogen generation rates of 302.8, 102.8, and 40.6mL min^{-1} g^{-1} recorded at 1.00, 1.50, and 2.00 wt% NaOH, respectively. These observations indicate that 0.50 wt% NaOH provides the optimum alkaline environment for Cu–Ti NPs during $NaBH_4$ hydrolysis. Initial increase at hydrogen evolution was due to enhanced activation of catalytic sites and accelerated desorption of $B(OH)_4^-$ intermediates. However, excessive alkalinity increases solution viscosity and promotes the accumulation of borate species at catalyst surface, partially blocking active sites and reducing the overall reaction rate.

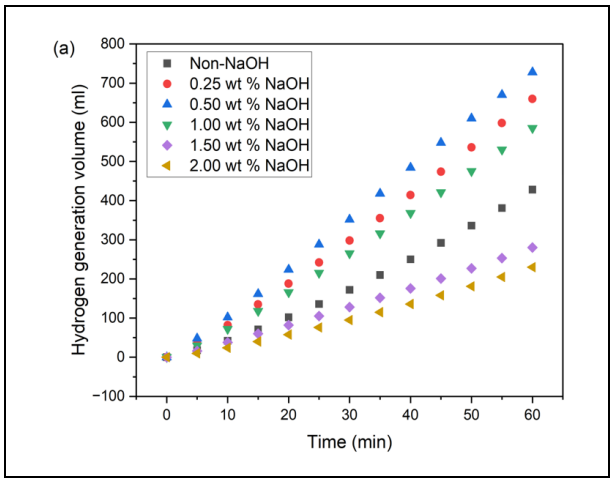

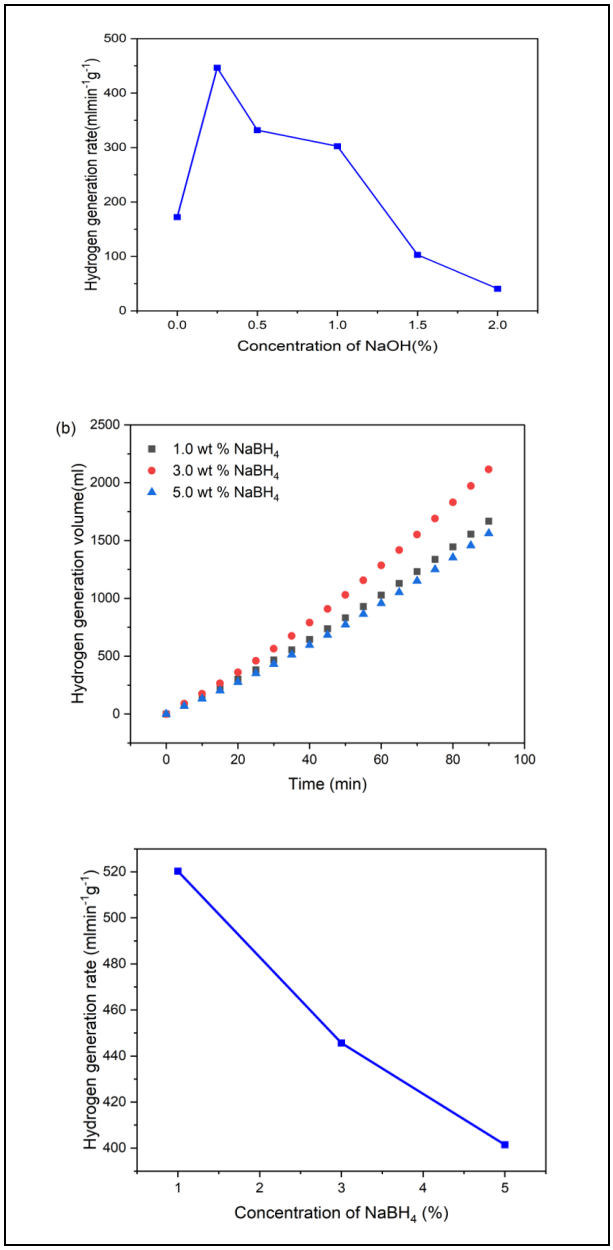

Fig. 2: Catalytic hydrolysis performance of (a) NaOH concentration effect and (b) $NaBH_4$ concentration effect

The addition of $NaBH_4$ on the catalytic hydrogen evolution of the synthesized Cu–Ti NPs was systematically evaluated using 1.0, 3.0, and 5.0 wt% $NaBH_4$ solutions, as presented in Fig. 2b. A further increase to 5.0 wt% resulted in a noticeable reduction in the hydrogen evolution rate. This decrease is primarily attributed to the formation and deposition of sodium metaborate on the catalyst surface together with the increased viscosity of the reaction medium, which restricts reactant diffusion and blocks accessible catalytic active sites. Consequently, 3.0 wt% $NaBH_4$ was identified as the optimum reactant concentration for efficient hydrogen production using the green-synthesized Cu–Ti NPs (Spurio *et al.* 2026).

The elevated $NaBH_4$ concentrations and continuous formation of sodium metaborate leads to deposition of reaction by-products at catalyst surface, thereby reducing number of active sites. In addition, the increased viscosity of the reaction medium restricts efficient mass transfer among reactants and catalyst, resulting in a lower hydrogen evolution rate. Furthermore, addition of catalyst loading on hydrogen production was systematically examined using 20, 40, 60, and 80 mg of the synthesized Cu–Ti NPs, and the results are presented in Fig. 3.

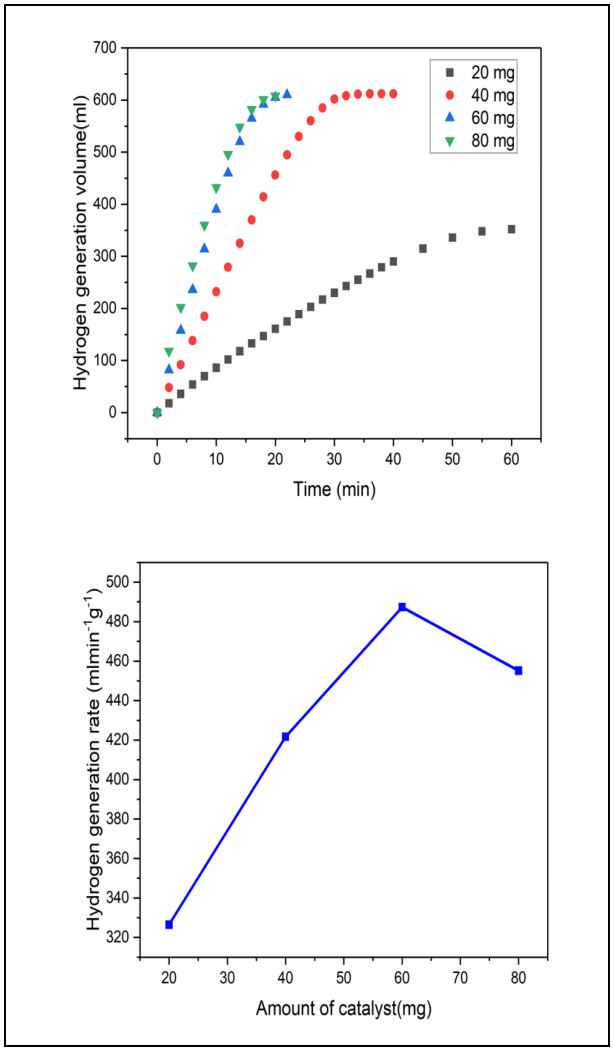

Fig. 3: Effect of catalyst dosage

Hydrogen generation performance during $NaBH_4$ hydrolysis was strongly influenced by the amount of Cu–Ti catalyst employed. Increasing the catalyst loading from 20 mg to 60 mg markedly enhanced the hydrogen evolution rate owing to higher availability of catalytically active sites. Enlarged active surface area promotes more efficient interaction between the reactants and the catalyst, thereby accelerating the hydrolysis reaction. As illustrated in Fig. 4, reaction completion time gradually decreased with increasing catalyst dosage, confirming that higher catalyst loadings resulted in faster hydrogen production kinetics.

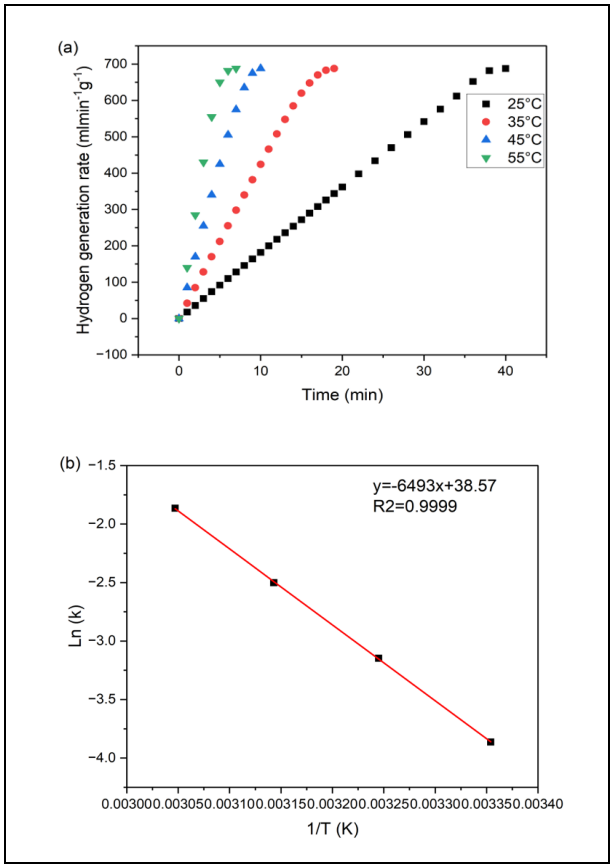

Fig. 4: (a) Temperature effect on catalysis and (b) Arrhenius plot analysis

Increasing the catalyst dosage to 80 mg caused a slight reduction in hydrogen generation rate compared with optimum loading of 60 mg. This behavior is mainly associated with particle agglomeration at higher catalyst concentrations, which decreases effective surface area and restricts accessibility of active catalytic sites. Local depletion of reactants around clustered nanoparticles further limits the hydrolysis process. These findings demonstrate that catalyst loading must be carefully optimized to achieve maximum hydrogen production efficiency. In addition, the catalytic performance of the synthesized Cu–Ti NPs was examined at 25, 35, 45, and 55 °C to investigate the influence of reaction temperature.

Hydrolysis of $NaBH_4$ catalyzed by synthesized Cu–Ti NPs was completed within approximately 40, 19, 10, and 7 minutes at 25, 35, 45, and 55 °C, respectively, as illustrated in Fig. 4a. The progressive reduction in reaction time with increasing temperature demonstrates that elevated temperatures accelerate hydrogen evolution by enhancing molecular kinetic energy and increasing the frequency of effective reactant–catalyst collisions. The Arrhenius analysis further confirmed that increasing temperature promotes the hydrolysis reaction by

lowering the kinetic barrier and increasing the reaction rate constant. Although higher temperatures improve catalytic activity, excessive thermal conditions may influence catalyst stability during prolonged operation. Therefore, identifying an optimum reaction temperature is essential for achieving both sustained catalyst performance and efficient hydrogen production. The observations confirm that temperature was the key operating parameter governing $NaBH_4$ hydrolysis. Reaction kinetics of $NaBH_4$ in the presence of Cu–Ti NPs was evaluated using the nth-order model and activation energy was determined from the Arrhenius eqn using data presented in Fig. 4b. In the absence of a catalyst, activation energy of $NaBH_4$ hydrolysis is approximately 245 kJ mol^{-1}. Green-synthesized Cu–Ti catalyst prepared using *Psidium guajava* leaf extract reduced the activation energy to approximately 53.98 kJ mol^{-1}, reaction order of n = 0.29. The reduced activation energy demonstrates the enhanced catalytic efficiency of the synthesized nanomaterial by facilitating the cleavage of B–H bonds during hydrolysis. Thus, the experimental outcomes provide insight into influence of reaction parameters on catalyst performance. Furthermore, integrating these experimental observations with machine learning models enables reliable prediction and optimization of hydrogen generation under different operating conditions.

3.3 Regression Model Performance Comparison

Machine learning has become an effective approach in chemical engineering for predicting nonlinear catalytic processes controlled by several interacting variables. Compared with conventional kinetic or models, ML methods recognize hidden relationships among reaction parameters without requiring a predefined mathematical equation. This is particularly useful for catalytic hydrogen generation, where hydrogen evolution strongly depends on catalyst composition, reaction temperature, alkaline concentration, catalyst loading, and reaction time.

This work predicts the hydrogen generation rate during $NaBH_4$ hydrolysis using green-synthesized Cu–Ti NPs prepared with *Psidium guajava* leaf extract. Integration of experimental data with regression-based machine learning models helps improve process understanding, identify important operating conditions, and reduce repeated experimental trials.

In this study, seven supervised regression algorithms were developed and compared using MATLAB, namely Gaussian Process Regression (GPR), Support Vector Regression (SVR), Random Forest Regression, Extra Trees Regressor, CatBoost Regressor, Light Gradient Boosting Machine (LightGBM) Regressor, and HistGradientBoosting Regressor. These models were selected because they can effectively handle nonlinear relationships, feature interactions, and complex catalytic behavior. Model optimization was carried out using grid-search-based parameter tuning with 5-fold cross-validation to minimize overfitting and avoid data leakage. The predictive performance was evaluated using R^2, MAE, RMSE, and MAPE, while Taylor diagrams were employed to evaluate prediction stability and model reliability. The developed models were applied only within the investigated experimental range and were not used for extrapolation beyond the studied conditions.

3.4 Data Preprocessing Workflow

Dataset used in work contained 288 experimental observations obtained from $NaBH_4$ hydrolysis using green-synthesized Cu-Ti NPs prepared with *Psidium guajava* leaf extract. The target output was the hydrogen generation rate (H_2 rate, mL min^{-1} $gcat^{-1}$), while input variables were temperature (T, °C), $NaBH_4$ concentration (C_{NaBH_4}, wt%), NaOH concentration (C_{NaOH}, wt%), Cu-Ti catalyst mass (mCuTi, g), and reaction time (t, s). The experimental ranges were 25-55 °C, 0-2.00 wt% NaOH, 1.0-5.0 wt% $NaBH_4$, 20-80 mg, catalyst, and the corresponding sampled reaction time.

Learning ability of MATLAB-based regression models was performed to represent nonlinear catalytic behavior. Polynomial terms such as t^2, t^3, and T^2 were generated, while transformed time variables including $\log(t+1)$ and $\sqrt{t}$ were added to describe saturation-type hydrogen evolution. Interaction features such as $T \times \log(t+1)$, $T \times mCuTi$, $\log(t+1) \times mCuTi$, $\sqrt{t} \times mCuTi$, and m^2CuTi were also included to capture catalyst-loading effects. In addition, an alkalinity-to-catalyst ratio was introduced to describe the relative alkaline strength with respect to catalyst dosage.

$$R_{alk/cat} = \frac{C_{NaOH}}{m_{CuTi}} \quad \ldots (4)$$

The proposed descriptor enables the regression models to generalize more effectively across different operating conditions by representing the relationship between the alkalinity of the reaction medium and the available catalyst loading. Prior to model development, input variables were normalized to [0, 1] range by Min-Max normalization technique, ensuring numerical consistency during training and preventing variables with magnitudes from disproportionately influencing learning process. The relationships among the original and engineered features were subsequently examined using the correlation matrix shown in Fig. 5, providing an overview of the dependencies between the constructed input variables.

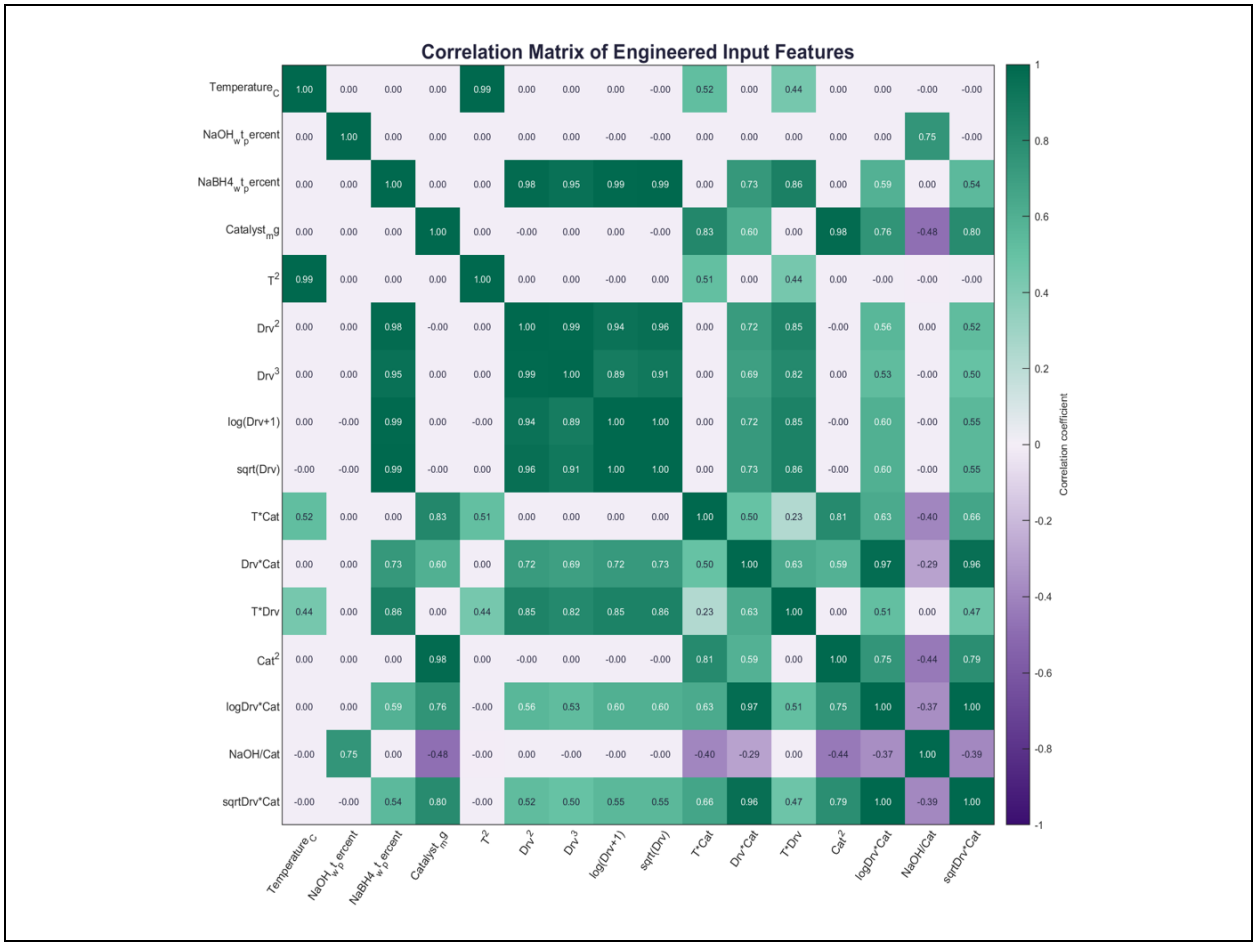

Fig. 5: Correlation matrix of engineered input features

Polynomial features generated from same input variable exhibited mutual correlations, particularly among t, t^2, and t^3, reflecting their common mathematical origin. Likewise, interaction among reaction temperature and Cu-Ti loading showed a high degree of correlation with catalyst dosage because both variables strongly influence the catalytic hydrolysis process. In contrast, descriptors such as the alkalinity-to-catalyst ratio (Ralk/cat) and m^2CuTi displayed comparatively weak correlations with the remaining predictors, indicating that they contribute additional independent information useful for model development.

Although feature engineering introduced a degree of multicollinearity, no predictors were removed because the selected regression algorithms are capable of effectively handling correlated variables through nonlinear learning, ensemble decision trees, or kernel-based optimization.

3.5 LightGBM Regression

Light Gradient Boosting Machine was efficient tree-based learning algorithm that used gradient boosting while adopting a histogram-based learning strategy to accelerate model training and reduce memory consumption. Unlike conventional boosting algorithms, LightGBM grows decision trees in a leaf-wise manner with depth constraints, enabling improved predictive accuracy and efficient handling of complex nonlinear relationships.

Because of its capability to model intricate feature interactions and large engineered feature sets, LightGBM was selected as one of the principal regression algorithms for predicting the hydrogen generation in the investigation.

The prediction model of LightGBM is formulated as:

$$F_m(x) = F_{m-1}(x) + \gamma_m h_m(x) \qquad \dots (6)$$

The predictive capability of the LightGBM model was assessed using 5-fold cross-validation, and corresponding prediction outcomes are presented in Fig. 6.

Predicted hydrogen rates exhibit excellent agreement with the experimental observations, demonstrating that LightGBM effectively captures nonlinear relationships among operating variables and

catalytic performance. The close correspondence among measured and predicted values confirms robustness and reliability of the developed model. These findings indicate that LightGBM is a powerful regression algorithm for modeling catalytic hydrogen evolution and that its leaf-wise boosting strategy combined with the engineered features, provides accurate and stable predictions across the investigated experimental conditions.

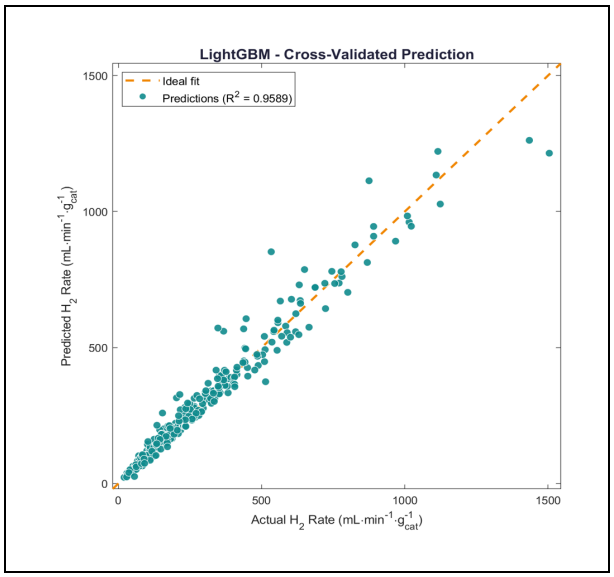

Fig. 6: LightGBM prediction performance

3.6 Gaussian Process Regression

Gaussian process regression is a non-parametric, probabilistic machine learning algorithm widely used for nonlinear regression because of its excellent predictive capability and inherent ability to quantify prediction uncertainty (Kaliyaperumal *et al.* 2026). Unlike conventional regression methods, GPR models the relationship between input and output variables using covariance (kernel) functions, enabling accurate prediction of complex nonlinear systems without assuming a predefined functional form. Owing to its flexibility and robustness, GPR is particularly suitable for experimental datasets with intricate feature interactions and relatively limited sample sizes.

In the present study, the GPR model was trained using the engineered feature dataset together with 5-fold cross-validation. Model hyperparameters, including the kernel function, kernel scale, signal variance, and noise variance, were optimized to improve prediction accuracy while maintaining strong generalization performance across the validation folds.

The predictive capability of the GPR model is showed in Fig. 7. Cross-validated predictions exhibit excellent agreement with experimental hydrogen generation, demonstrating that developed model effectively represents the nonlinear behavior governing $NaBH_4$ hydrolysis. The optimized GPR model reached highest predictive performance among all investigated algorithms, with an R^2 value of 0.9937, confirming its excellent prediction accuracy and strong generalization capability.

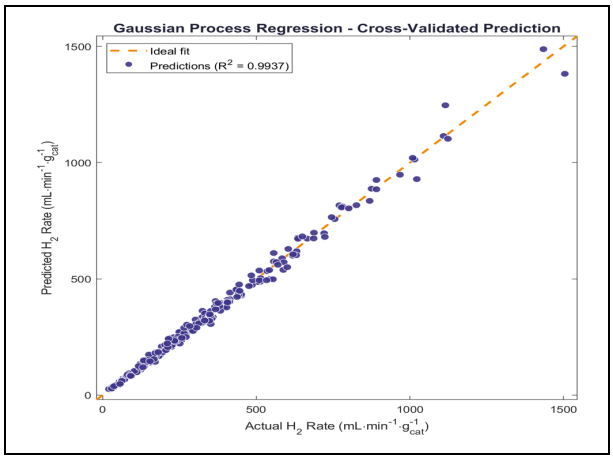

Fig. 7: GPR prediction performance

To further interpret the ML results, the relative predictor importance obtained from the HistGradientBoosting Regressor is presented in Fig. 8. Although GPR provided the highest predictive accuracy, HistGradientBoosting was employed for interpretability because tree-based ensemble models enable reliable estimation of predictor importance.

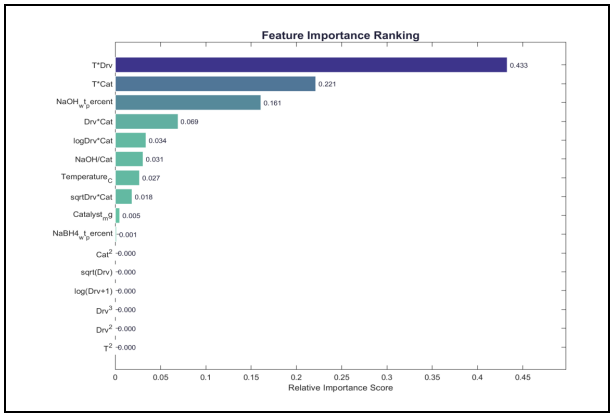

Fig. 8: Relative predictor importance obtained from HistGradientBoosting regressor

The predictor importance analysis indicates that the engineered interaction variables, particularly T × Drv and T × Cat, together with NaOH concentration, contributed most significantly to hydrogen generation prediction. These findings demonstrate effectiveness of the adopted feature-engineering approach and are consistent with catalytic kinetics of $NaBH_4$ hydrolysis, where reaction temperature, catalyst loading, and alkaline concentration collectively influence hydrogen evolution.

3.7 Comparative Model Evaluation

The evaluation was carried out using multiple statistical performance indicators, enabling a comprehensive assessment of prediction accuracy, robustness, and model reliability. Furthermore, the predictive capability of each algorithm was examined through comparative performance analysis, while predictor importance and interpretability analyses were performed to provide deeper insight into the influence of the experimental variables governing the hydrogen generation process.

3.7.1 Regression Evaluation Metrics

To ensure a comprehensive and objective comparison of the developed regression models, four standard statistical performance metrics were used. The evaluation criteria that collectively assess different aspects of predictive performance, including goodness of fit, average prediction error, relative percentage deviation, and sensitivity to large residuals were selected. Multiple statistical measures provide a balanced and reliable assessment while minimizing potential bias associated with interpreting model performance using a single metric.

- **Coefficient of Determination** (R^2) : The R^2 evaluates proportion of variance in observed hydrogen generation rate was explained by the regression model. An R^2 value approaching 1 indicates excellent agreement between the predicted and experimental data.

$$R^2 = 1 - \frac{\sum_{i=1}^{n} (y_i - \hat{y}_i)^2}{\sum_{i=1}^{n} (y_i - \bar{y})^2} \quad \dots (7)$$

- **Mean Absolute Error:** MAE average absolute variation among predicted and measured values provides direct measure of prediction accuracy without disproportionately weighting large errors.

$$MAE = \frac{1}{n}\sum_{i=1}^{n} |y_i - \hat{y}_i| \quad \dots (8)$$

- **Mean Absolute Percentage Error:** The prediction error as percentage of observed value, allowing model performance to be compared independently of the data scale.

$$MAPE = \frac{100}{n}\sum_{i=1}^{n} \left|\frac{y_i - \hat{y}_i}{y_i}\right| \quad \dots (9)$$

- **Root Mean Squared Error (RMSE):** The RMSE estimates the standard deviation of the prediction errors by assigning greater weight to larger residuals, making it particularly useful for identifying models with substantial prediction deviations.

$$RMSE = \sqrt{\frac{1}{n}\sum_{i=1}^{n} (y_i - \hat{y}_i)^2} \quad \dots (10)$$

3.7.2 Regression Performance Comparison

To comprehensively evaluate predictive capability of regression models, comparative assessments were performed by four statistical indicators, namely MAE, R^2, MAPE and RMSE.

Performance results summarized in Table 1 indicate that all developed regression models provided satisfactory predictive performance for hydrogen generation rate estimation. Investigated approaches, Gaussian Process Regression reached highest prediction accuracy, followed by LightGBM, CatBoost, SVR, and HistGradientBoosting Regressor. These models effectively captured the nonlinear relationships governing catalytic hydrogen generation, whereas Extra Trees and Random Forest exhibited comparatively lower predictive performance because of the complex interactions among the engineered features.

Table 1. Regression metrics comparison

Model	R^2	MAE	RMSE	MAPE (%)
Gaussian Process Regression	0.993729	12.3138	19.819	4.590564
LightGBM	0.958914	29.30036	50.72843	11.01194
CatBoost	0.958426	29.95866	51.02886	10.78729
Support Vector Regression	0.958327	30.59786	51.08971	15.14115
HistGradientBosting	0.954935	30.68948	53.12844	11.20925
Extra Trees Regressor	0.882391	57.8994	85.8274	23.518
Random Forest Regression	0.851046	65.48443	96.59005	26.98269

The GPR model produced highest R^2 value (0.9937) together with the lowest MAE (12.31 mL min^{-1} $gcat^{-1}$) and RMSE (19.81), confirming its excellent capability to describe the nonlinear behavior of the hydrogen generation process while maintaining strong generalization during cross-validation. LightGBM also demonstrated outstanding predictive performance with only a marginal reduction in accuracy, followed by CatBoost, which effectively captured the interactions among the engineered variables. The SVR and HistGradientBoosting Regressor provided reliable predictions with moderate error levels, whereas Extra Trees and Random Forest exhibited comparatively lower

predictive performance because of the complex interactions among the engineered features.

To further validate model performance, Fig. 9 shows scatter plots comparing the predicted and experimental hydrogen generation obtained using 5 cross-validation.

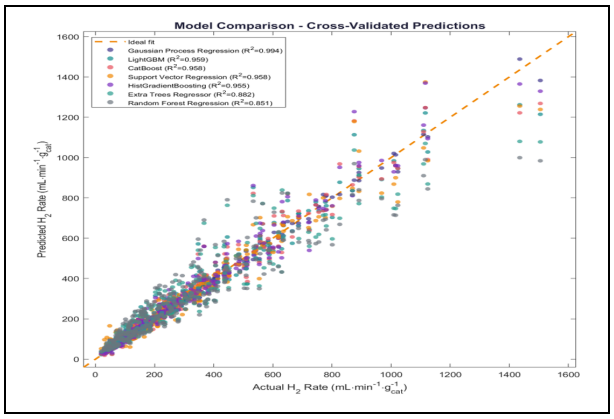

Fig. 9: Cross-validation prediction results

In addition, Taylor graph shown in Fig. 10(a and b) simultaneously compares the correlation coefficient, centered RMSE, and standard deviation for all investigated algorithms, providing a comprehensive visualization of model agreement with the experimental data.

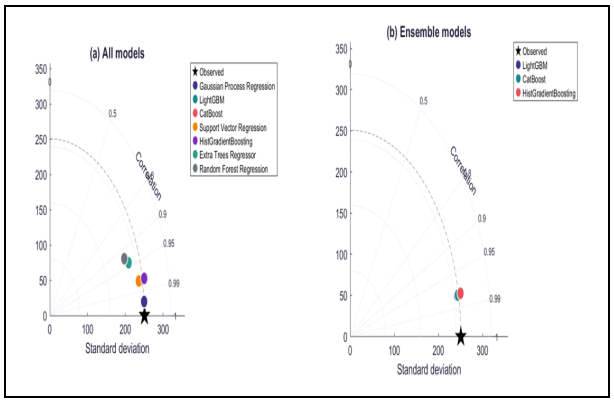

Fig. 10: Regression performance comparison

Overall, the comparative analysis demonstrates that GPR, LightGBM, and CatBoost consistently delivered the highest prediction accuracy, robustness, and stability, making them the most suitable algorithms for modeling hydrogen generation from $NaBH_4$ hydrolysis using green-synthesized Cu–Ti NPs. A previous study reported that a biogenic N-doped Fe–Zn–Bi trimetallic nanocomposite synthesized using *Psidium guajava* leaf extract was effectively modeled using a Modified CatBoost Regressor, which achieved the highest predictive accuracy. The model successfully captured the nonlinear relationships governing petroleum hydrocarbon degradation, demonstrating excellent robustness and generalization capability (Sarma *et al.* 2025).

3.7.3 Predictor Importance Analysis

Although prediction accuracy was essential for evaluating regression models, interpretability is also important in catalytic hydrogen generation because it helps relate model outputs to reaction behavior. In this study, model interpretation was performed using predictor importance analysis obtained from the HistGradientBoosting Regressor. Although Gaussian Process Regression achieved the highest predictive accuracy, HistGradientBoosting was selected for interpretation because tree-based ensemble models provide reliable predictor importance estimates.

The predictor importance results showed that the interaction features T × Drv and T × Cat, together with NaOH concentration, were the most influential variables affecting hydrogen generation. This agrees with the kinetic behavior of $NaBH_4$ hydrolysis, where temperature, catalyst loading, and alkaline concentration strongly influence hydrogen evolution.

The relative predictor importance analysis demonstrates that the engineered interaction variables effectively captured the nonlinear relationships among the reaction parameters, confirming the effectiveness of adopted feature engineering strategy.

Thus, the MATLAB-based interpretability results confirm that the HistGradientBoosting Regressor provides valuable interpretability and chemically meaningful insight into the key factors controlling hydrogen evolution.

4. CONCLUSION

In this work, Cu–Ti bimetallic NPs was fabricated by *Psidium guajava* leaf extract natural reducing, capping, and stabilizing agent *via* an eco-friendly synthesis process. Their catalytic activity toward hydrogen evolution through $NaBH_4$ hydrolysis was systematically investigated under different operating conditions. Furthermore, artificial intelligence-driven machine learning models were implemented to predict and optimize hydrogen generation performance, enabling a comprehensive evaluation of the relationships between reaction variables and catalytic efficiency.

Green-mediated synthesis successfully produced well-crystallized Cu–Ti bimetallic NPs with an average crystallite dimension of approximately 40 nm. The synthesized catalyst exhibited its maximum hydrogen evolution efficiency at a sodium hydroxide concentration of 0.50 wt%. The catalytic performance was comprehensively assessed by varying key operational parameters, including reaction temperature, catalyst loading, and $NaBH_4$ concentration. Kinetic

evaluation indicated that the hydrolysis process followed an nth order reaction mechanism, and the corresponding activation energy was determined to be 53.98 kJ mol^{-1}. To further enhance the analysis, the experimental dataset was interpreted using several machine learning regression algorithms. Among the evaluated models, GPR delivered the highest prediction accuracy, whereas the HistGradientBoosting Regressor effectively quantified the relative importance of the experimental variables governing hydrogen generation. Validation through 5-fold cross-validation confirmed the robustness and generalization capability of the developed predictive models. In particular, the GPR model achieved the best overall performance with an R^2 of 0.9937. In addition, the Taylor diagram revealed excellent correspondence between the measured and predicted hydrogen production values, together with a low centered root-mean-square error, showing reliability and predictive capability of machine learning framework over the investigated experimental range.

The findings of this investigation confirm that plant-assisted synthesized Cu–Ti bimetallic nanoparticles possess significant potential as efficient catalysts for hydrogen generation through sodium borohydride hydrolysis. The integration of systematic experimental evaluation with machine learning-driven predictive modeling proved to be an effective strategy for understanding and improving catalytic performance under different operating conditions. The proposed methodology offers a practical framework for catalyst optimization and can be readily adapted to other environmentally synthesized nanocatalysts and broader reaction environments. Expanding this approach with larger experimental datasets and diverse catalyst systems is expected to facilitate the development of more accurate, robust, and transferable predictive models, thereby supporting the advancement of sustainable hydrogen production technologies.

FUNDING

This research received no specific grant from any funding agency in the public, commercial, or not-for-profit sectors.

CONFLICTS OF INTEREST

The authors declare that there is no conflict of interest.

COPYRIGHT

This article is an open-access article distributed under the terms and conditions of the Creative Commons Attribution (CC BY) license (http://creativecommons.org/licenses/by/4.0/).

REFERENCES

Abdellatif, M. M., Eliwa, H. A., El Degwy, M. A. A. E. A., Shabana, S., Nassif, R. M., Mohamed, H. S. and Abdelmonem, R., Botanical Nanofiber Wound Dressing Loaded with Psidium guajava Leaf Extract: Preparation, Characterization, and In Vivo Evaluation, *Pharma.*, 18(1), 31(2026). https://doi.org/10.3390/pharmaceutics18010031

Akhil, R. T., Alice, N. A., Mydhili, V., Prakash, D., Manivannan, S. and Girisun, T. C. S., Near-resonant excited state enhanced optical limiting in stable rGO/Cu nanocomposites, *Diamond Related Mater.*, 160, 113018(2025). https://doi.org/10.1016/j.diamond.2025.113018

Akram, S., Hussain, S., Arif, M., Ali, M. H., Tariq, M., Rauf, A., Munawar, K. S., Alkahtani, H. M., Alhaj Zen, A. and Ali, S. S. A., *Psidium guajava* mediated green synthesized cobalt oxide nanoparticles dispersed on reduced graphene oxide for electrocatalytic water splitting, *RSC Adv.*, 15(18), 13786–13798 (2025). https://doi.org/10.1039/d5ra00040h

Alsalamah, S. A., Alawlaqi, M. M., Sumayli, M., Areshi, S. M., Hazzazi, Y., Alghonaim, M. I. and Almotayri, A. M., Ecofriendly Production of CuO/ZnO Nanocomposites from Guava Leaf Biomass and their Antimicrobial and Selective Anticancer Activities, *BioRes.*, 21(2), 2906–2924 (2026). https://doi.org/10.15376/biores.21.2.2906-2924

Balasubramaniyan, G., Senthilkumar, G., Rahman, M. A. and Sasi, B., Bio-Inspired Synthesis of Dual Oxide-Alginate Nanocomposites Using Guava Leaf Extract for Antibacterial and Anticancer Applications, *J. Cluster Sci.*, 36(6), 232(2025). https://doi.org/10.1007/s10876-025-02956-2

Begum, S. K., Shabnam, D., Haque, N., Alam, M. J., Ferdous, J., Nur, U. J. B., Fatema, K., Shabiha, R. J., Clarke, R. J., Chowdhury, P. and Uddin, M. N., Green synthesis of magnetite (Fe_3O_4) and hematite (Fe_2O_3) nanoparticles using Moringa oleifera and Psidium guajava leaf extracts for sustainable applications, *Sci. Rep.*, 15(1), 36465(2025). https://doi.org/10.1038/s41598-025-21603-4

Bui, T. L., Hejazi, S. M. H., Navrátil, J., Kmentová, H., Bábor, P., Henrotte, O., Mascaretti, L., Bisetto, M., Sanders, S. K., Schirato, A., Otyepka, M., Błoński, P., Montini, T., Zboril, R., Fornasiero, P., Alabastri, A., Naldoni, A. and Kment, S., Non-Thermal-Driven Photocatalytic Ammonia Decomposition at Near-Room Temperature on a Plasmonic Nanocone Array, *Adv. Func. Mater.*, 36(21), e05216(2026). https://doi.org/10.1002/adfm.202505216

Dokania, P., Maity, S., Nancharaiah, Y. V and Sarkar, A., Development of Novel Green Synthesized Chitosan Doped nZVI Nanocomposite and Its Synergistic Antibacterial and Anti-biofilm Activity Against Marine Bacteria Isolated from Nuclear Power Plant, *J. Inorg. Organomet. Polym. Mater.*, 36(2), 1610–1631 (2026). https://doi.org/10.1007/s10904-025-04005-x

Ganesan, M., Jeice, A. R. and Rajaram, P., Influence of Annealing Calefactions on Nickel Oxide Nanoparticles Bio-Fabricated Using Psidium guajava Leaves Extract: In-Vitro Antimicrobial Features, *High Energy Chem.*, 59(5), 444–453(2025). https://doi.org/10.1134/S0018143925700298

Goyal, S., Ballal, S., Punia, A., Sharma, D., Nagpal, M., Pathak, J., Thangavelu, I. and Tadepalli, S., Biocidal Activity of Barium and Iron-Co-Doped Titanium Dioxide Nanocomposites, Synthesized by Psidium guajava-Mediated Precipitation Method, *Biotechnol. Appl. Biochem.*, 73(4), 2068-2078(2026). https://doi.org/10.1002/bab.70155

Hema, K., Anishia, S. R., Rajeswari, S., Padmavathy, V., Sujatha, S. and Thiyagu, M., Green synthesis and Multifunctional Applications of *Moringa Oleifera* - enhanced TiO_2 Nanocomposites, *J. Environ. Nanotechnol.,* 14(1), 7-17(2025). https://doi.org/10.13074/jent.2025.03.2511225

Iqbal, A., Pati, S. K. and Thapa, R., Identification of an Electronic Descriptor for Interpreting CO2ER toward C2 Product Formation on Cu NP-Based Alloys, *ACS Appl. Energy Mater.*, 9(8), 4910–4922(2026). https://doi.org/10.1021/acsaem.6c00110

Jagadeesha, A. V., Zhengyou, L., Yadav, K. K., Alqhtani, H. A., Nasr, F. A., Alreshidi, M. A., Pattar, V., Novikov, E. and Aldosari, F. M., Synergistic band-gap engineering and electrochemical performance of $Cu_{1-x}Zn_xFe_2O_4$ spinel ferrites synthesized via dual-fuel solution combustion for high-performance supercapacitors and alkaline electrocatalysis, *J. Energy Storage*, 153, 120837(2026). https://doi.org/10.1016/j.est.2026.120837

Kaliyaperumal, V., Vajravelu, S. K., Justin, A. and Maruthaiah, T., Identification of abiotic stress in Psidium guajava plant sample using LIBS method combined with machine learning approach, *Appl. Phy. A: Mater. Sci. Proce.*, 132(1), 2(2026). https://doi.org/10.1007/s00339-025-09166-7

Kim, M. J., Jeon, I. J., Xia, Y., Ku, B. J., Kim, M., Jang, W. J., Lee, K., Guo, J. and Shim, J. O., Cu behavior and catalytic properties on highly distributed CeO_2-MgO supports: Impact of Cu loading in HTS reactions for waste-to-hydrogen production, *Appl. Catal. A: General*, 708, 120584(2025). https://doi.org/10.1016/j.apcata.2025.120584

Lin, S., Yan, K., Sun, Z., Zhang, Z., Lan, Y., Wang, L. and Zhang, Y., Non-destructive prediction of soluble solids content and firmness and maturity determination of guava fruit using color and fluorescence imaging, *Postharvest Bio. Technol.*, 227, 113620(2025). https://doi.org/10.1016/j.postharvbio.2025.113620

Mathew, D., Thomas, B., Sudheep, N. M., Varghese, S., Yesudas, V., Thomas, J. B. and Radhakrishnan, E. K., Psidium guajava Leaf Phytochemical-Assisted One-Step Synthesis of Metformin/ZnO Nanoconjugate for Enhanced Solubility, Hydrophilicity, Biocompatibility, and Broad-Spectrum Therapeutic Potential, *J. Clust. Sci.*, 37(4), 100(2026). https://doi.org/10.1007/s10876-026-03057-4

Mohamed, M. V, Ahamed, A. J., Begum, A. S., Alharbi, H. M., Khojah, A. A., Ahamed, F. M. M., Sarkar, S., Almohaimeed, H. M. and Uti, D. E., Investigation of the anticancer, antibacterial, and photocatalytic properties of CeO_2 and Cu-CeO_2 nanoparticles synthesized by a green method, *Green Chem. Lett. Rev.*, 18(1), 2543911(2025). https://doi.org/10.1080/17518253.2025.2543911

Naseer, H., Iqbal, T., Afsheen, S. and Ali, A. M., Novel green synthesis of magnesium–titanium–zinc trimetal oxide nanocomposites as heterogeneous photocatalysts for antibacterial activities and shelf life applications, *European Phy. J. Plus*, 138(8), 763(2023). https://doi.org/10.1140/epjp/s13360-023-04387-2

Noorani, A. H., Khan, M. K., Ahmad, M. F. A., Ahmad, S. A., Khan, Z. and Ansari, N., Green-synthesized CuO/rGO nanocomposite with enhanced visible-light response for textile dye Photodegradation under natural sunlight, *Inorg. Chem. Commun.*, 188(P2), 116526(2026). https://doi.org/10.1016/j.inoche.2026.116526

Raghupathy, S., Sivalingam, A. M., Brahma, N. and Alex, A., Phytochemical Analysis of Silver Nanoparticles of Psidium guajava Leaf Extract and Evaluation for Its Antibacterial Property, *J. Pharm. Bioallied Sci.*, 16(Suppl 2), S1256–S1262 (2024). https://doi.org/10.4103/jpbs.jpbs_565_23

Rahman, M. H., Hossen, A. and Mondal, M. I. H., A multifunctional aspect of surface modification of cotton fabric with green synthesized titanium dioxide/iron nanocomposite using Psidium guajava leave extract, *J. Tex. Insti.*, 116(8), 1743–1753(2025). https://doi.org/10.1080/00405000.2024.2398355

Ran, M., Wu, J., Jiao, Y. and Li, J., Efficient removal of Sb(III) from wastewater using selenium nanoparticles synthesized by Psidium guajava plant extract, *Environ. Sci. Pollut. Res*, 31(31), 43781–43797 (2024). https://doi.org/10.1007/s11356-024-34007-0

Saeed, K., Zada, N. and Khan, I., Photocatalytic degradation of alizarin red dye in aqueous medium using carbon nanotubes/Cu–Ti oxide composites, *Separat. Sci. Technol. (Philadelphia)*, 54(16), 2729–2737(2019). https://doi.org/10.1080/01496395.2018.1552296

Sarma, N., Rabha, S., Baruah, N. P., Rahman, T., Goswami, T., Mahanta, L. B. and Devi, A., Combined biogenic-trimetallic nanocomposite for advanced visible-light-driven photodegradation of total petroleum hydrocarbons orchestrated by machine learning, *Surf. Interf.*, 70, 106835(2025). https://doi.org/10.1016/j.surfin.2025.106835

Sathiyavimal, S., Vasantharaj, S., Veeramani, V., Saravanan, M., Rajalakshmi, G., Kaliannan, T., Al-Misned, F. A. and Pugazhendhi, A., Green chemistry route of biosynthesized copper oxide nanoparticles using Psidium guajava leaf extract and their antibacterial activity and effective removal of industrial dyes, *J. Environ. Chem. Eng.*, 9(2), 105033(2021). https://doi.org/10.1016/j.jece.2021.105033

Shingole, M. R., Mula, S., Singh, K. K., Kumar, A., Meena, S. S., Ruz, P. and Banerjee, S., Cu/Fe_3O_4 embedded polyethersulfone beads: a scalable and magnetically separable catalyst for hydrogen evolution from ammonia borane and selective hydrogenation of cinnamaldehyde, *J. Mater. Chem. A*, 14(22), 13707–13723 (2026). https://doi.org/10.1039/d5ta09853j

Soundarya, R., Kiruthika, K., Rathishkumar, S., Sugumaran, S., Kamakshi, K. and Sekhar, K. C., Microwave assisted green synthesis of copper nanoparticles for enhanced photocatalytic, photothermal, and antibacterial applications, *Next Nanotechnol.*, 9, 100534(2026). https://doi.org/10.1016/j.nxnano.2026.100534

Spurio, E., Alimonti, F., Bertoni, G., D'Addato, S., Ammirati, G., Paladini, A., Turchini, S., Catone, D., O'Keeffe, P. and Luches, P., Morphology, local stoichiometry, and photoexcited states in Cu@Cu_2O nanostructured systems grown by physical synthesis, *J. Chem. Phy.*, 164(12), 124702(2026). https://doi.org/10.1063/5.0309793

Tuyen, N. N. K., Dat, N. M., Dat, T. D. and Hieu, N. H., Preparation and characterization of biodegradable films based on chitosan/poly(vinyl alcohol) incorporating selenium-immobilized graphene oxide for fruit preservation, *Chem. Pap.*, (2026). https://doi.org/10.1007/s11696-026-05051-6

Warkad, S., Sangeetha Gowda K., R., Mirajkar, K. K., More, S. S., Mudhish, E. A., Mahnashi, M. H., Maashi, M. H., Shaikh, I. A., Khan, A. A., Muddapur, U. M., More, V. S., Khan, A. A. and Hussain, M. G., Green Synthesis of Silver Nanoparticles and Fluconazole Hybrid Nanoformulations for Managing Fusarium oxysporum Wilt Disease in Chickpea Plants, *Chem. Select*, 11(12), e04721(2026). https://doi.org/10.1002/slct.202504721